actuators

MDPI

Article

MEC-Based Modeling and Design of Permanent Magnet Synchronous Machines with Axial–Radial Rotor Extensions Using Yoke and Rotor-Side Spaces

Soheil Yousefnejad *, Majid Mehrasa * and Parviz Rastgoufard

Electrical Engineering Department, University of New Orleans, 2000 Lakeshore Drive, New Orleans, LA 70148, USA; prastgou@uno.edu
* Correspondence: syousefn@uno.edu (S.Y.) and mmehrasa@uno.edu (M.M.)

Abstract

This paper proposes a solution to enhance the torque production capability of Permanent Magnet Synchronous Machine (PMSM), utilizing not only the unused space resulting from the stator end windings on the rotor side, but also the otherwise unused space around the winding on the yoke side. By implementing an additional axial rotor equipped with Permanent Magnets (PMs) in both rotor and yoke sides, the proposed design technique increases the PMSM torque output, taking advantage of the useless space on the yoke side. In the proposed configuration, one magnetic flux path circulates between the PMs on the rotor (rotor side) and the stator, while an additional flux path circulates between the PMs positioned on both sides of the stator end windings. These two flux paths contribute to generating a stronger and more effective magnetic field within the machine than conventional structure, resulting in increased torque density. A magnetic equivalent circuit (MEC) model of the proposed design is developed, and its accuracy is validated through Finite Element (FE) analysis. For a fair evaluation, the proposed structure is compared with a conventional configuration using the same volume of PM material. Furthermore, optimization of the proposed design is carried out to maximize Torque/PM.

Keywords: permanent magnet synchronous machine; axial-assist magnets; torque enhancement; stator end windings; yoke side

check for updates

Academic Editor: Tobias Hemsel

Received: 22 August 2025
Revised: 2 October 2025
Accepted: 6 October 2025
Published: 20 October 2025

Citation: Yousefnejad, S.; Mehrasa, M.; Rastgoufard, P. MEC-Based Modeling and Design of Permanent Magnet Synchronous Machines with Axial–Radial Rotor Extensions Using Yoke and Rotor-Side Spaces. *Actuators* **2025**, *14*, 507. https://doi.org/10.3390/act14100507

Copyright: © 2025 by the authors. Licensee MDPI, Basel, Switzerland. This article is an open access article distributed under the terms and conditions of the Creative Commons Attribution (CC BY) license (https://creativecommons.org/licenses/by/4.0/).

1. Introduction

To date, several methods have been proposed to improve torque production and reduce the torque ripple. In [1], the rotor's edge shape is optimized using the third harmonic principles to boost torque production. Similarly, in [2,3], the PM shape is modified to align with the third harmonic waveforms along the radial axis, leading to higher average torque and lower torque ripple. The use of sinusoidal and the third harmonic-shaped PMs along axial axis, as documented in [4,5], may help reduce torque ripple and cogging torque while achieving a more sinusoidal voltage waveform. Additionally, combining sinusoidal and the third harmonic shaping techniques along the radial axis, as explored in [6,7], may reduce surface torque ripple while maintaining high output torque. Another effective solution to enhance torque density is the use of Halbach array PMs as documented in [8]. Similar approach is extended to coaxial, axial, and linear magnetic geared machines in [9–12].

Dual-stator structures offer several advantages. First, they allow for better distribution of the magnetic field, which enhances torque production. Second, the use of two stators

helps balance the torque more effectively, leading to smoother operation. Third, this design makes more efficient use of the available motor space, often enabling more compact designs while still achieving high performance [13,14].

The PMs extension along the axial axis—known as the overhang structure—enhances the torque deliver, as documented in [15–17]. In this configuration, the overall size of the motor remains unchanged, but additional PMs are placed along the rotor's axial axis to strengthen the magnetic field. This design utilizes otherwise unused space in the machine, which exists due to the stator's end windings. In the conventional (non-overhang) structure of a PMSM, the airgap is uniform. However, in the overhang structure, implementing axial PMs alters the airgap in the overhang section depending on its length. Although this structure increases magnet utilization, it also results in a larger airgap.

To enhance the torque output and improve the operational flexibility, a Radial–Axial Brushless Hybrid Excitation Machine (RA-BHEM) is proposed and studied. The machine integrates both radial and axial magnetic circuits, featuring a radial stator with armature windings and an axial stator with AC excitation windings. This configuration allows for independent control of excitation without brushes or slip rings, significantly improving system reliability. The hybrid excitation—consisting of PMs and controllable axial excitation—enables flexible flux regulation to enhance torque performance [18].

The airgap flux density of a hybrid flux PMSM is enhanced by combining the radial and axial flux paths and using integrated windings. An overhang PM structure and additional magnetic cores are also added to further improve power density. The machine's stator and rotor both include axial and radial components. The stator cores are laminated in directions matching their respective flux paths and are combined into a single structure, with integrated coil windings placed in the unified stator slots [19].

Extending the PMs along the axial direction—commonly referred to as the overhang structure—enhances torque performance, as reported in [15–17]. In this configuration, the overall size of the motor remains unchanged; instead, PMs are added to the rotor's axial end to boost the magnetic field. This approach takes advantage of the unused space in the machine, typically resulting from the stator's end windings [16,20,21]. In conventional (non-overhang) PMSM designs, the airgap is uniform. However, in the overhang structure, adding axial PMs changes the airgap size in the overhang area based on how long the overhang is. While this improves magnet utilization, it also leads to an increase in the airgap.

A synchronous machine with doubly salient structures and PMs embedded in the stator yoke have been developed in [22]. In that design, the stator incorporates PMs in a special configuration, while the rotor remains unchanged, resulting in an increased torque density. The magnet is implemented in stator yoke; however, in the proposed structure, the stator configuration remains unchanged, and instead, the otherwise unused space caused by the stator end windings—on both the rotor and yoke sides—is utilized. This unused space is often neglected in conventional designs, and the present work aims to address this limitation.

To calculate the no-load back-EMF of the machine, several studies have employed the magnetic equivalent circuit (MEC) model for both Surface PMSMs and Interior PMSMs [16,17,21,23–26]. In [16,17,21,24–26], the rotor features an overhang structure, and the MEC model is developed to achieve accurate back-EMF results in comparison with FEM simulations.

In this paper, a novel axial overhang structure is proposed, which utilizes both sides of the stator end windings—toward the rotor side and the yoke side. By placing PMs in these regions, the airgap magnetic field is intensified, leading to increased induced voltage and, consequently, higher torque. The performance characteristics of the proposed

structure, including torque and back-EMF voltage, are analyzed through Finite Element (FE) simulations. Additionally, a MEC model is developed, and its results are compared with those obtained from FE analysis to validate the accuracy of the analytical model.

2. General Topology

Figure 1 illustrates the flux path of the conventional model in the non-overhang section. In this figure, color lines can be described as the following [25]:

- The blue line represents the flux passing through the magnet and rotor. The blue flux path (ϕ_{mr}) corresponds to the reluctance shown in blue (R_{mrr}).
- The purple line in Figure 1a represents the flux flowing between the magnets, the airgap, and the rotor core. The purple flux path (ϕ_{mm} in Figure 1a) corresponds to the reluctance shown in purple in Figure 1b(R_{mmr}).
- The green line represents the flux flowing between the magnets on the same side of the rotor, the stator core, and the rotor core. The green flux path (ϕ_g) corresponds to the reluctances shown in green (R_{gr}, R_{sr}, and R_{rr}).

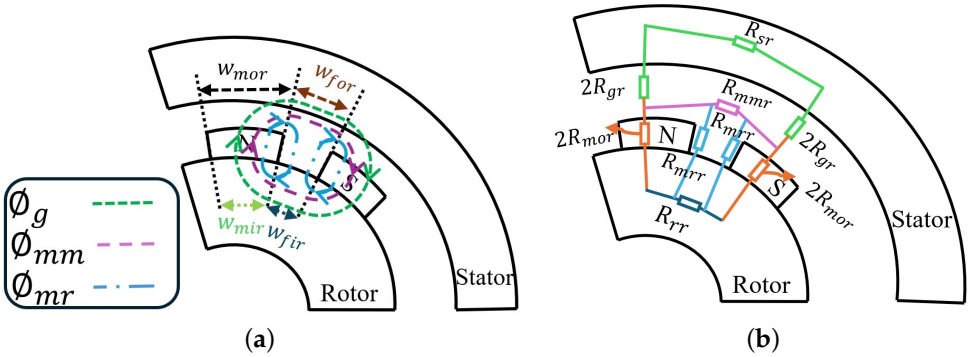


Figure 1. XY-plane cross-section of the PMSM structure for (**a**) non-overhang section and (**b**) reluctance of the area.

In this paper, a novel axial overhang structure is proposed, which takes advantage of both sides of the stator end windings—toward the rotor side and the yoke side—as illustrated in Figure 2. In this design, an axial rotor is added to the conventional non-overhang structure. The axial rotor contains two sets of PMs: one on the rotor side and one on the yoke side, both magnetized in the axial direction.

The flux path of the rotor side PMs is shown in purple and circulates through the rotor side PMs, the rotor core, and the stator core. The yellow flux line represents the magnetic path involving both rotor side and yoke side PMs, passing through the rotor side PMs, rotor core, yoke side PMs, and stator core. The third type of flux path, shown in black, corresponds to the magnetic flux generated by the PMs in the non-overhang (conventional) section, passing through the radial PMs, radial rotor core, and stator core.

These flux lines are all aligned in the same direction within the airgap, meaning they reinforce one another and collectively increase the airgap flux. As a result, the back-EMF and torque of the machine are significantly enhanced.

The proposed PMSM machine is shown in Figure 2a which has two rotors, axial rotor (Figure 2b) and radial rotor. It should be noted that the magnetization direction of the PM in the axial and radial rotor should be axial and radial, respectively. The main design parameters are listed in Table 1.

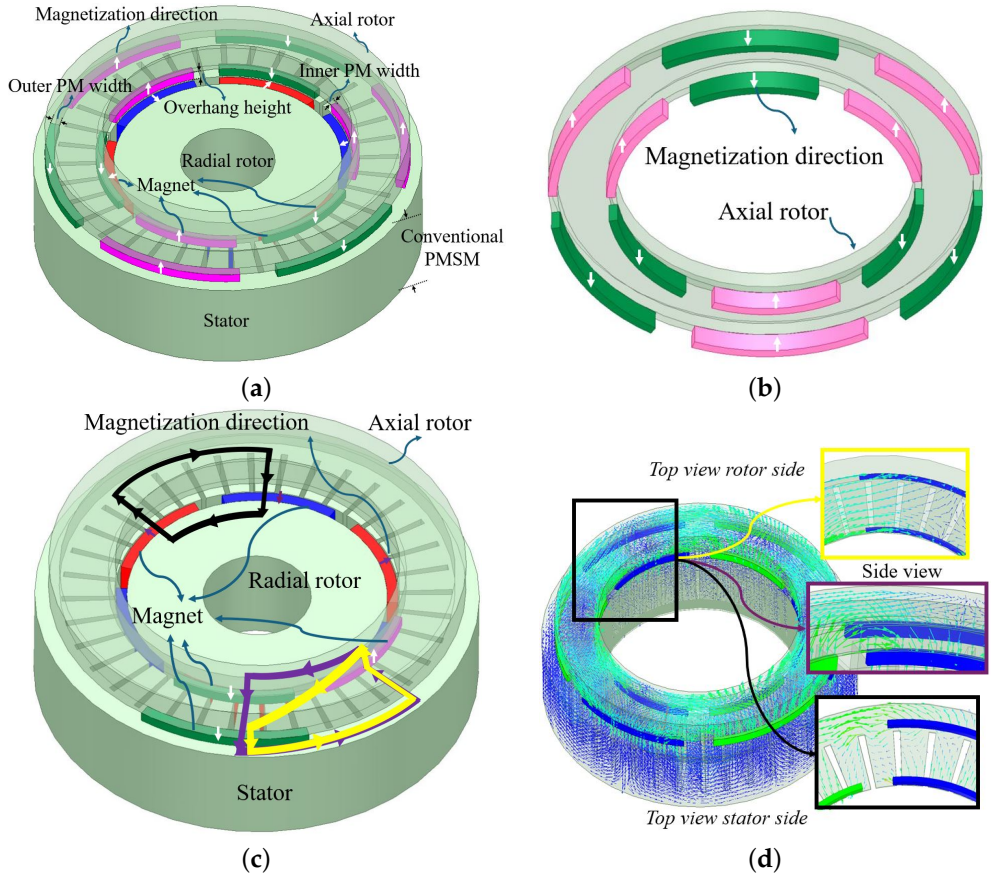


Figure 2. PMSM machine. (**a**) Whole configuration with PM magnetization directions. (**b**) Axial rotor with PM magnetization directions. (**c**) Effective flux lines. (**d**) Flux lines in FEM simulation.

Table 1. Design Parameters.

Parameters	Dual-Stator PMSM
Axial length (mm)	40
Overall radius (mm)	82
Radial airgap length (mm)	0.5
Axial airgap length adjacent to inner PM (mm)	0.5
Axial airgap length adjacent to outer PM (mm)	0.5
No. of phase	3
No. of stator slot	36
No. of pole pairs	3
No. of conductor	50
Inner rotor PM width (mm)	0.6
Outer rotor PM width (mm)	1.1
Rotor PM height (mm)	0.6
Radial rotor PM outer radius (mm)	52
Radial rotor PM inner radius (mm)	48
Axial rotor core height (mm)	14
Axial rotor core width (mm)	4
Axial rotor core inner radius (mm)	52.5
Axial rotor core outer radius (mm)	74
Axial rotor inner PM inner radius (mm)	52.5
Axial rotor Outer PM outer radius (mm)	74
Magnet Flux Density	1.07T
Core material	steel 1010

According to the flowchart presented in Figure 3 , the proposed MEC model is implemented in this study as follows:

1. The magnetic flux in the non-overhang section of the conventional PMSM is calculated using the MEC model, and it is shown as the black line in Figure 2c (black window in Figure 2d).
2. The magnetic field of the axial overhang flux is analyzed based on the proposed MEC model, and its corresponding magnetic field is depicted by the yellow and purple lines in Figure 2c (yellow and purple window in Figure 2d).
3. The combined model is applied to account for the effect of the stator tooth, as referenced in [16].

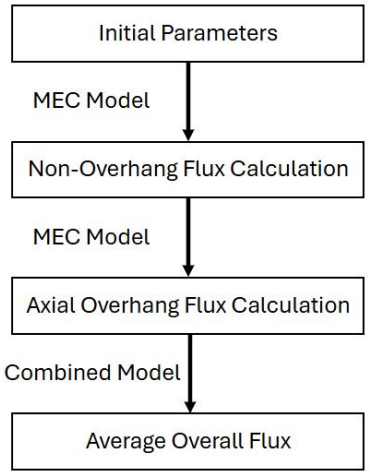


Figure 3. Flowchart of the magnetic field calculation in the proposed machine.

Figure 4 illustrates the side view of the proposed structure from the X-Z cross-section. It also highlights the flux path, which is essential for constructing the MEC model. Figure 5 illustrates the MEC of the conventional PMSM, where the magnetization direction of the PMs is radial. In the proposed structure, an additional rotor is introduced, with the PMs magnetized axially. This axial magnetization reduces the effective airgap compared to the conventional overhang design. The MEC model of the proposed structure is presented in this section and is depicted in Figure 6.

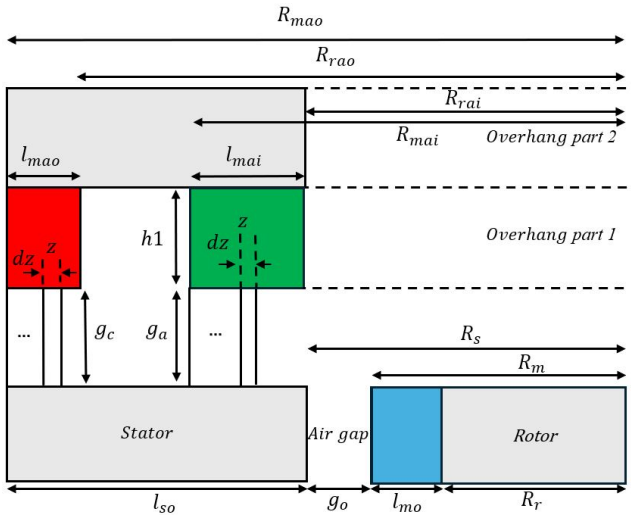


Figure 4. Modeling of the magnetic flux in the airgap between the stator core and overhang parts (Half of the motor's cross-sectional view along the x-z axis).

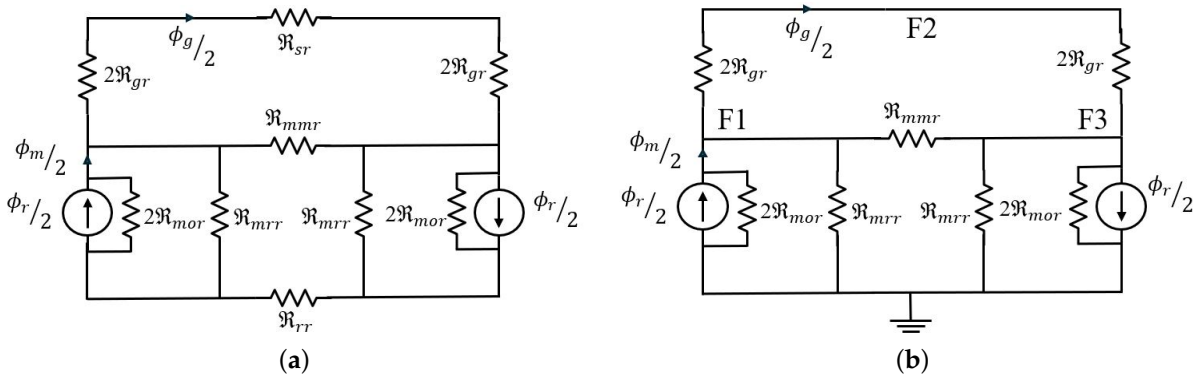


Figure 5. The MEC model of the proposed model in the (**a**) non-overhang section [21] (radial rotor section) (**b**) with neglected stator and rotor reluctances.

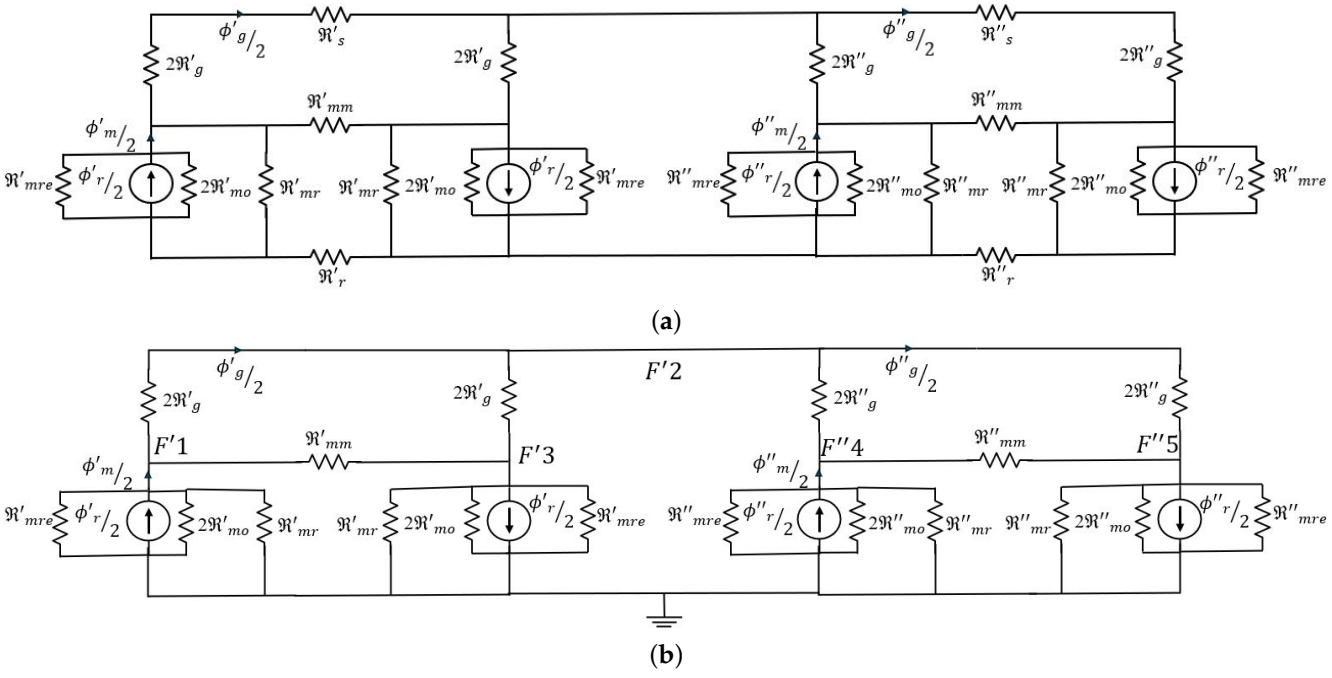


Figure 6. The MEC model of the proposed configuration in the (**a**) axial rotor structure (**b**) with neglected stator and rotor reluctances.

$$
\begin{aligned}
w_{mir} &= \frac{\pi\alpha_p}{p}\left(\frac{R_r + R_m}{2}\right), & w_{fir} &= \frac{\pi(1-\alpha_p)}{p}\left(\frac{R_r + R_m}{2}\right),\\
w_{mor} &= \frac{\pi\alpha_p}{p}\left(\frac{R_s + R_m}{2}\right), & w_{for} &= \frac{\pi(1-\alpha_p)}{p}\left(\frac{R_s + R_m}{2}\right),\\
w_{mai} &= \frac{\pi\alpha_p}{p}\left(\frac{R_{rai} + R_{mai}}{2}\right), & w_{fai} &= \frac{\pi(1-\alpha_p)}{p}\left(\frac{R_{rai} + R_{mai}}{2}\right),\\
w_{may} &= \frac{\pi\alpha_p}{p}\left(\frac{R_{rao} + R_{mao}}{2}\right), & w_{fay} &= \frac{\pi(1-\alpha_p)}{p}\left(\frac{R_{rao} + R_{mao}}{2}\right)
\end{aligned}
\tag{1}
$$

The reluctance of the flux path of the MEC model of the radial rotor (non-overhang section) is shown as follows [16]:

The reluctance corresponding to ϕ_{gr} (R_{gr}), shown in Figure 1, and R_{mor} can be calculated using the fundamental equation of magnetic reluctance. The fringing effect in R_{gr} is also taken into account by adding the length $2g_o$ to w_m in the calculation of R_g [23].

$$
R_{gr} = \frac{g_o}{\mu_0(w_{mor} + 2g_o)l_{st}} \tag{2}
$$

$$R_{mor} = \frac{l_{mo}}{\mu_0 \mu_r w_{mir} l_{st}} \tag{3}$$

The expression for R_{mrr} and R_{mmr} can be derived by first calculating its permeance. Among the available approaches, the circular-arc straight-line permeance model is one of the most effective techniques for modeling flux in an airgap and is used here to calculate R_{mrr} and R_{mmr} [23].

$$R_{mmr} = \frac{\pi}{\mu_0 l_{st} \ln(1 + \frac{\pi g_o}{w_{for}})} \tag{4}$$

$$R_{mrr} = \frac{\pi}{\mu_0 l_{st} \ln(1 + \frac{\pi g_o}{l_{mo}})} \tag{5}$$

In the axial rotor, R'_g and R''_g are the same as those in the non-overhang section, with the fringing effect also taken into account. Similarly, R'_{mo} and R''_{mo} can be calculated using the fundamental equation of magnetic reluctance, as in the non-overhang section. The permeance models for the magnet-to-magnet paths (R'_{mm} and R''_{mm}) and the magnet-to-rotor paths (R'_{mr} and R''_{mr}) in the axial rotor are also the same as those in the non-overhang section, except that the radial parameters are replaced with the corresponding axial parameters. Then, the reluctance of the MEC model of the axial rotor in the outer and inner sections is shown as follows:

$$R'_g = \frac{g_a}{\mu_0 (w_{mai} + 2g_a) l_{mai}} \tag{6}$$

$$R'_{mo} = \frac{h_1}{\mu_0 \mu_r w_{mai} l_{mai}} \tag{7}$$

$$R'_{mr} = \frac{\pi}{\mu_0 l_{mai} \ln(1 + \frac{\pi g_a}{h_1})} \tag{8}$$

$$R'_{mm} = \frac{\pi}{\mu_0 l_{mai} \ln(1 + \frac{\pi g_a}{w_{fai}})} \tag{9}$$

$$R''_g = \frac{g_c}{\mu_0 (w_{may} + 2g_c) l_{mao}} \tag{10}$$

$$R''_{mo} = \frac{h_1}{\mu_0 \mu_r w_{may} l_{mao}} \tag{11}$$

$$R''_{mr} = \frac{\pi}{\mu_0 l_{mao} \ln(1 + \frac{\pi g_c}{h_1})} \tag{12}$$

$$R''_{mm} = \frac{\pi}{\mu_0 l_{mao} \ln(1 + \frac{\pi g_c}{w_{fay}})} \tag{13}$$

The end effects resulting from the leakage flux between the magnet and the rotor end can be neglected in non-overhang SPM machines. However, these effects become significant when an overhang structure is adopted [16]. Therefore, the reluctance associated with this flux is calculated as R'_{mre}, and similar as R''_{mre}.

Here, the designations distinguished by the index ‘ (single prime) indicate the rotor side reluctances, while those distinguished by the index ‘‘ (double prime) indicate the yoke side reluctances, respectively.

$$R'_{mre} = \frac{\pi/2(h_1 + 3l_{mai} - 3z)}{\mu_0 w_{mai} dz} \tag{14}$$

$$R''_{mre} = \frac{\pi/2(h_1 + 3l_{mao} - 3z)}{\mu_0 w_{may} dz} \tag{15}$$

The stator and rotor core reluctances in the non-overhang section, R_{sr} and R_{rr}, are neglected as they are considered negligible [16]. For the same reason, the reluctances R'_r and R'_s, representing the rotor and stator core reluctances in the axial rotor on the magnet side, as well as R''_r and R''_s, representing those on the yoke side, are also neglected.

To calculate the flux of the radial rotor, the MEC model is shown in Figure 5a. By deriving the A matrix from the reluctances of the magnetic circuit, the flux of the radial rotor can be calculated as follows [16]:

$$\begin{aligned} G_{\mathrm{gr}} &= \frac{1}{2R_{gr}}, \quad G_{\mathrm{mor}} = \frac{1}{2R_{mor}}, \\ G_{\mathrm{mrr}} &= \frac{1}{R_{mrr}}, \quad G_{\mathrm{mmr}} = \frac{1}{R_{mmr}} \end{aligned} \tag{16}$$

$$G_{11} = G_{33} = G_{\mathrm{gr}} + G_{\mathrm{mor}} + G_{\mathrm{mrr}} + G_{\mathrm{mmr}} \tag{17}$$

$$\begin{aligned} &G_{12} = G_{21} = -G_{\mathrm{gr}}, \quad && G_{13} = G_{31} = -G_{\mathrm{mmr}}, \\ &G_{22} = 2G_{\mathrm{gr}}, && G_{23} = G_{32} = -G_{\mathrm{gr}}, \\ &G_{13} = G_{31} = -G_{\mathrm{mmr}} \end{aligned} \tag{18}$$

$$A = \begin{pmatrix} G_{11} & G_{12} & G_{13} \\ G_{21} & G_{22} & G_{23} \\ G_{31} & G_{32} & G_{33} \end{pmatrix} \tag{19}$$

In order to solve the magnetic circuit equations in the radial rotor, the flux density of the PM should be considered. The nodes F1, F2, and F3 are shown in Figure 5, and the formulation is given as follows [16]:

$$\varphi_{rr} = B_{ri} l_{st} w_{\mathrm{mir}} \tag{20}$$

$$F = \begin{pmatrix} F1 \\ F2 \\ F3 \end{pmatrix} \tag{21}$$

$$\phi = \begin{pmatrix} \phi_{rr}/2 \\ 0 \\ -\phi_{rr}/2 \end{pmatrix} \tag{22}$$

Then, the flux density of the radial airgap is calculated as follows [16]:

$$A.F = \Phi \tag{23}$$

In this study, to calculate the flux of the axial rotor, a magnetic circuit for the axial rotor is proposed. As shown in Figure 6a, to analyze the magnetic circuit, the A′ matrix is constructed as follows:

$$\begin{aligned} G'_{\mathrm{g}} &= \frac{1}{2R'_g}, \quad G'_{\mathrm{mo}} = \frac{1}{2R'_{mo}}, \quad G'_{\mathrm{mr}} = \frac{1}{R'_{mr}}, \\ G'_{\mathrm{mm}} &= \frac{1}{R'_{mm}}, \quad G'_{\mathrm{mre}} = \frac{1}{R'_{mre}}, \quad G''_{\mathrm{g}} = \frac{1}{2R''_g}, \\ G''_{\mathrm{mo}} &= \frac{1}{2R''_{mo}}, \quad G''_{\mathrm{mr}} = \frac{1}{R''_{mr}}, \quad G''_{\mathrm{mm}} = \frac{1}{R''_{mm}}, \\ G''_{\mathrm{mre}} &= \frac{1}{R''_{mre}} \end{aligned} \tag{24}$$

$$G'_{11} = G'_{33} = G'_{\mathrm{g}} + G'_{\mathrm{mo}} + G'_{\mathrm{mr}} + G'_{\mathrm{mm}} + G'_{\mathrm{mre}} \tag{25}$$

$$\begin{aligned} G'_{12} &= G'_{21} = -G'_{\mathrm{g}}, \quad G'_{13} = G'_{31} = -G'_{\mathrm{mm}}, \\ G'_{22} &= 2G'_{\mathrm{g}} + 2G'_{\mathrm{g}}, \quad G'_{23} = G'_{32} = -G'_{\mathrm{g}}, \\ G''_{14} &= G''_{41} = 0, \quad G''_{15} = G''_{51} = 0 \end{aligned} \tag{26}$$

$$G''_{44} = G''_{55} = G''_{\mathrm{g}} + G''_{\mathrm{mo}} + G''_{\mathrm{mr}} + G''_{\mathrm{mm}} + G''_{\mathrm{mre}} \tag{27}$$

$$\begin{aligned} G''_{42} &= G''_{24} = -G''_{\mathrm{g}}, \quad G''_{45} = G''_{54} = -G''_{\mathrm{mm}}, \\ G''_{25} &= G''_{52} = -G''_{\mathrm{g}} \end{aligned} \tag{28}$$

$$A' = \begin{pmatrix} G'_{11} & G'_{12} & G'_{13} & G''_{14} & G''_{15} \\ G'_{21} & G'_{22} & G'_{23} & G''_{24} & G''_{25} \\ G'_{31} & G'_{32} & G'_{33} & G''_{34} & G''_{35} \\ G''_{41} & G''_{42} & G''_{43} & G''_{44} & G''_{45} \\ G''_{51} & G''_{52} & G''_{53} & G''_{54} & G''_{55} \end{pmatrix} \tag{29}$$

As shown in Figure 6b, in the axial rotor, the effects of the flux from both the inner and outer PMs should be considered to calculate the flux density in the axial airgap. The fluxes of the inner and outer PMs are formulated as follows:

$$\varphi'_r = B'_r \, l_{mai} \, w_{\mathrm{mai}}, \quad \varphi''_r = B''_r \, l_{mao} \, w_{\mathrm{may}} \tag{30}$$

$$F' = \begin{pmatrix} F'1 \\ F'2 \\ F'3 \\ F''4 \\ F''5 \end{pmatrix} \tag{31}$$

$$\phi' = \begin{pmatrix} \phi'_r/2 \\ 0 \\ -\phi'_r/2 \\ \phi''_r/2 \\ -\phi''_r/2 \end{pmatrix} \tag{32}$$

Then, the flux density of the axial airgap is calculated as follows:

$$A'.F' = \Phi' \tag{33}$$

From the MEC model, the average magnetic flux density must be determined for two sections:

- Non-overhang (Equation (23)).
- Axial overhang (Equation (33)).

After determining the average flux density, the final step involves incorporating the combined model [16] to account for the effects of the stator slots.

3. Results

As shown in Table 2, the proposed MEC model is validated through FEM using different parameter values of the machine, which provides the advantage of saving both energy and time. This efficiency ensures that the design of the proposed structure requires significantly less time.

Table 2. Computation time and peak values of the no-load back-EMF calculation for the synchronous machine with the proposed and conventional overhang structures using the proposed model and 3D FEM (Computer configuration: 64 GB RAM, Core i9 3.20 GHz CPU).

h_1 (mm)	l_{mai} (mm)	l_{mao} (mm)	Proposed Model (V)	3D FEM (V)
4	1	1	18.71	18.86
4	1	2	18.83	18.71
4	2	1	19.10	19.25
4	2	2	19.35	19.06
8	1	1	18.74	18.91
8	2	1	19.14	19.29
8	1	2	18.85	18.71
8	2	2	19.40	19.15

The back-EMF waveform of a surface PM motor is obtained from the no-load flux density distribution and the armature winding distribution, as explained in [27]. The back-EMF voltages of the proposed MEC model and the 3D FEM over time are shown in Figure 7, demonstrating that the two curves closely match each other.

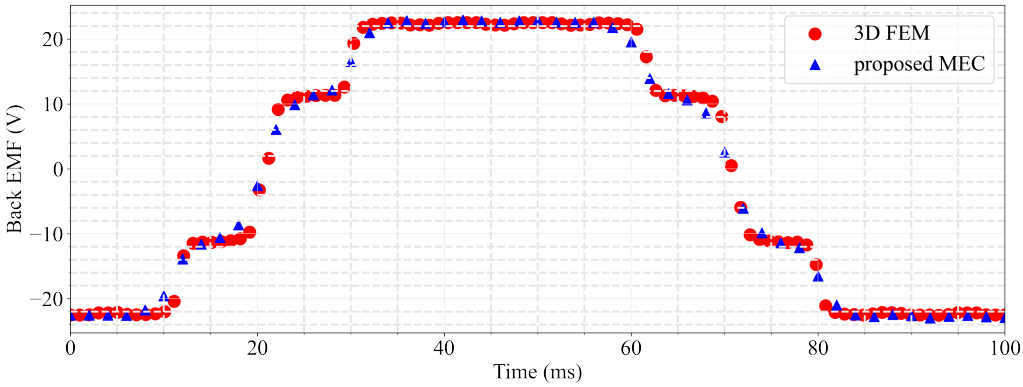


Figure 7. Back-EMF of 3D FEM and proposed model based on time (h_1 = 4 mm, l_{mai} = 1 mm, l_{mao} = 1 mm).

As shown in Figure 8, the overhang height has a greater impact on the torque per PM volume compared to the radius of the PMs on both the rotor and yoke sides.

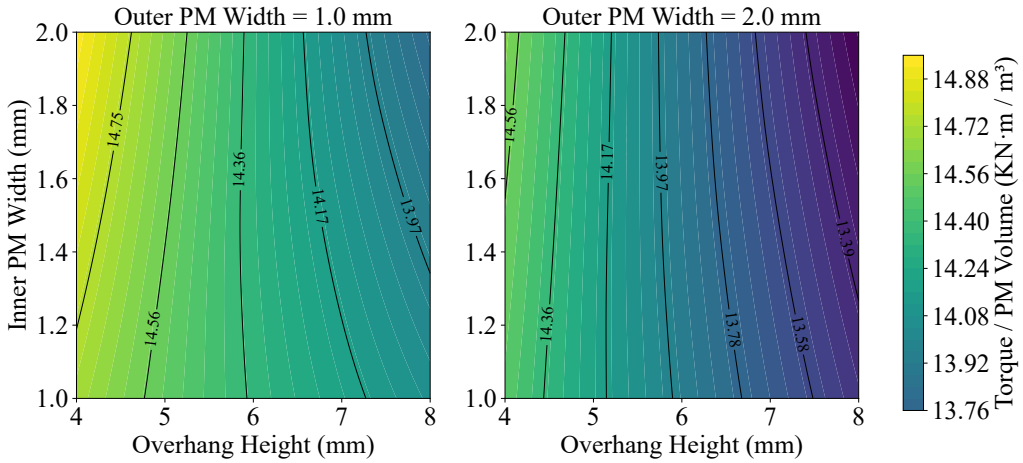


Figure 8. Torque per PM versus overhang inner radius (rotor side), outer radius (yoke side), and height (stator current = 1 A).

According to the flowchart presented in Figure 9a, the proposed structure is optimized as follows:

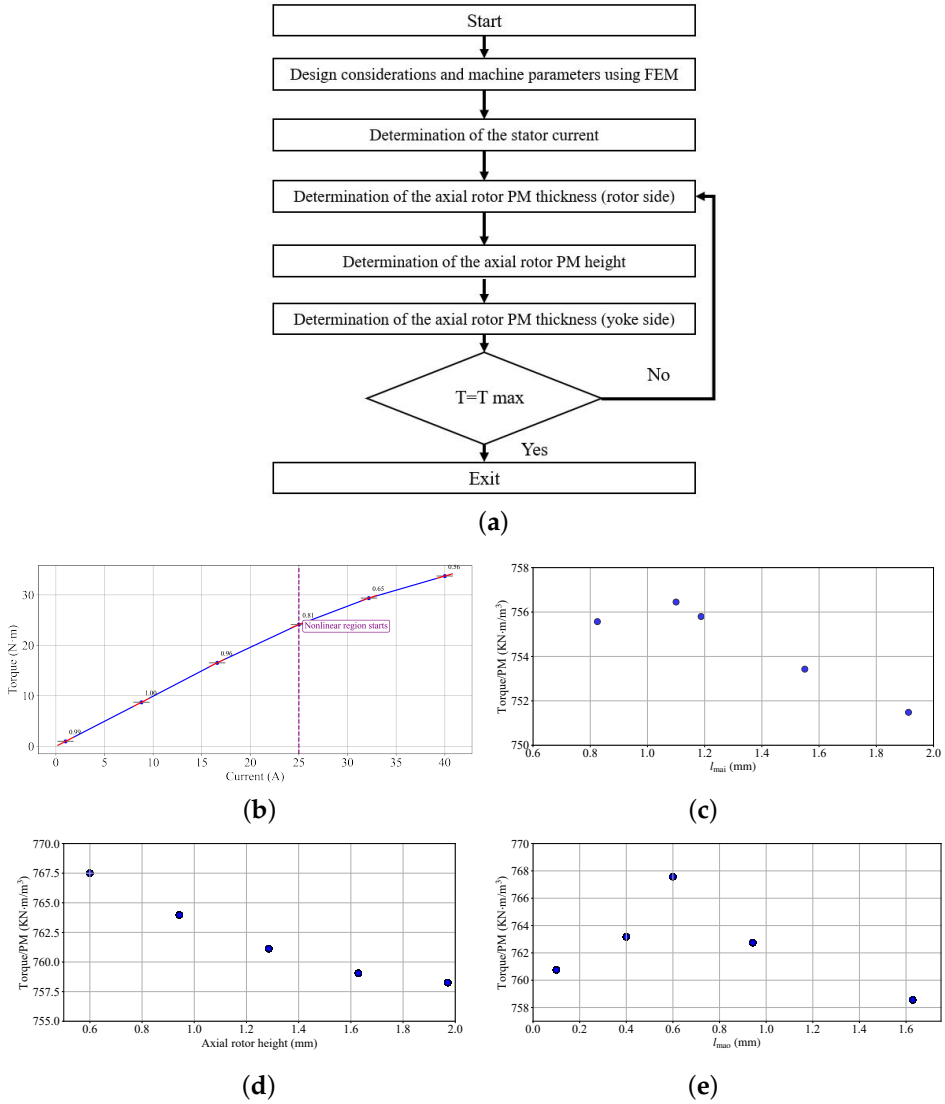


Figure 9. (**a**) Optimization flowchart of the proposed machine; (**b**) Torque–current curve with knee point at 25 A; (**c**) Torque versus axial rotor PM thickness on rotor side; (**d**) Torque versus axial rotor PM height; (**e**) Torque versus axial rotor PM thickness on yoke side.

To determine the knee point of the stator current, Figure 9b illustrates that the knee point of the torque-stator current curve occurs at 25 A.

As shown in Figure 9c, the torque-to-PM ratio of the machine is maximized when the PM width on the inner side of the rotor is 1.1 mm.

In this step, as shown in Figure 9d, the height of the axial rotor is determined based on the torque-to-PM ratio. Accordingly, the height is selected as 0.6 mm.

In the last step, as it is shown in Figure 9e, the PM width on the yoke side of the rotor is 0.6 mm.

As shown in Figure 10, the torque comparison in 1 A and 25 A, among the non-overhang structure (magnet width increased from 4.2 mm to 4.6 mm), the conventional overhang structure (magnet width increased from 4.2 mm to 4.6 mm with a magnet overhang length of 0.1mm to 0.6 mm), and the proposed structure (inner rotor PM width of 0.6 mm, outer rotor PM width of 1.1 mm, and rotor PM height increased from 0.6 mm to 6 mm) as a function of PM volume demonstrates that the proposed structure achieves a higher torque/PM than its counterparts within the magnet-volume range.

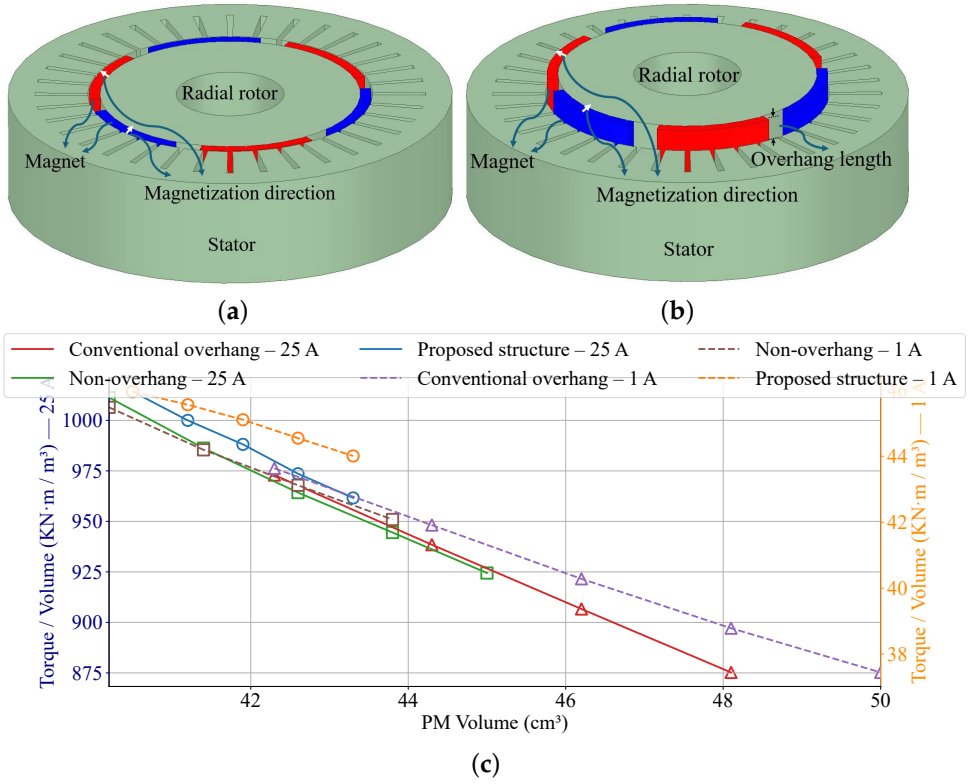


Figure 10. PMSM configuration with (**a**) non-overhang, (**b**) conventional overhang, and (**c**) torque comparison between the conventional overhang and non-overhang and proposed structure versus the PM volume at different current levels.

The analysis of the proposed structure in terms of efficiency, power factor, losses, torque ripple, core loss, flux linkage, and back-EMF is presented in Figure 11.

The back-EMF waveforms of the structures for PM volumes of 4.26×10^{-5} (Case 1) m^3 and 4.33×10^{-5} m^3 (Case 2) are presented in Figure 11g. As shown, the amplitude of the main harmonic of the back-EMF in the proposed machine increases with the PM volume. Moreover, for the same PM volume, the proposed structure achieves a higher main harmonic of the back-EMF compared to both the non-overhang and overhang structures.

As shown in Figure 11f, the flux linkage of the proposed machine increases with the PM volume. Moreover, for the same PM volume, the proposed structure achieves a higher flux linkage than both the non-overhang and overhang structures.

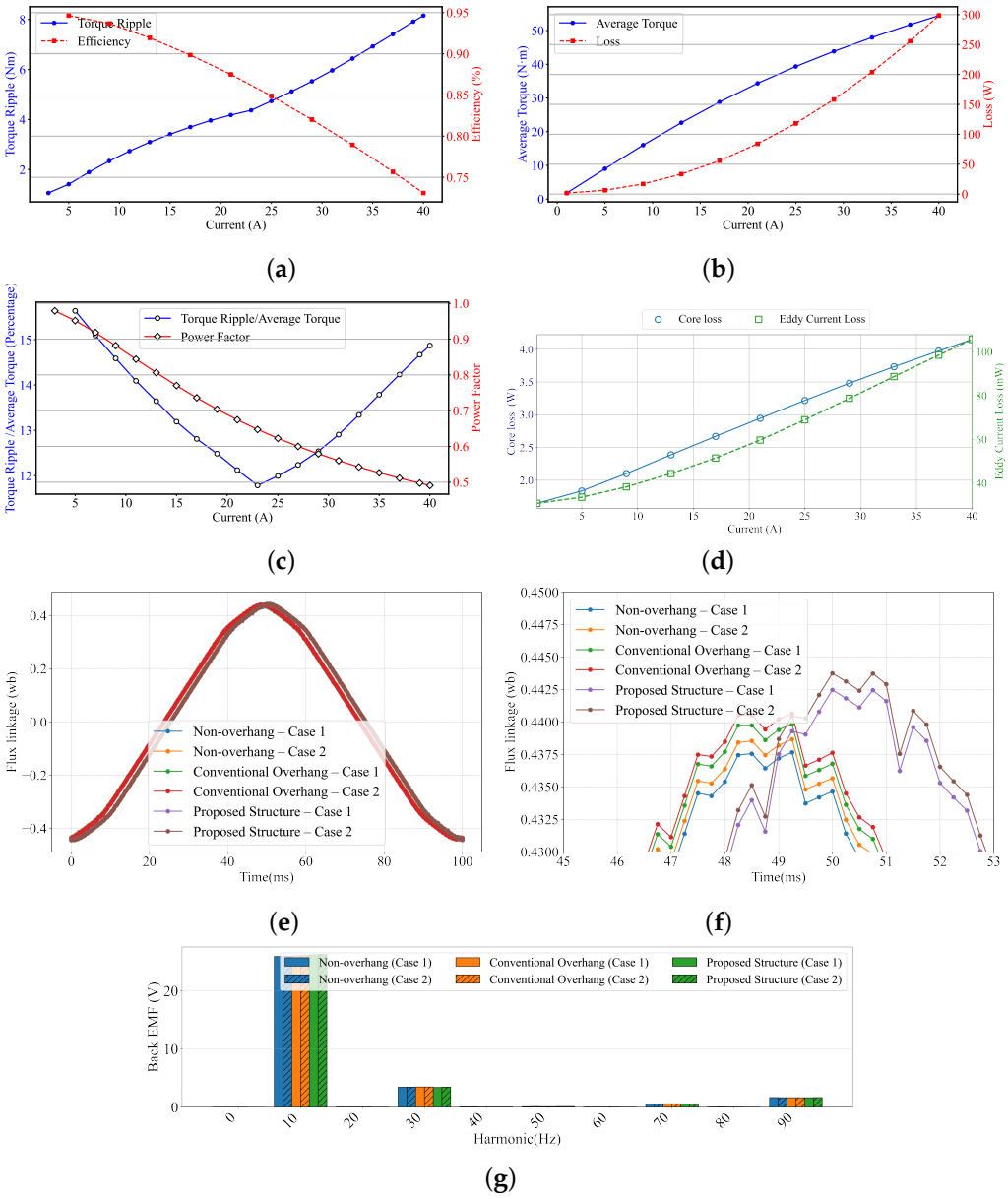


Figure 11. (**a**) Torque ripple and efficiency versus current. (**b**) Mean torque and whole loss versus current. (**c**) Torque ripple/mean torque and power factor versus current. (**d**) Core loss and eddy current loss versus current. (**e**) Flux linkage versus time. (**f**) Detailed flux linkage versus time. (**g**) Back-EMF voltage versus time.

Table 3 shows the cogging torque of the proposed machine in comparison with other counterparts for the same PM volume.

Table 3. Comparison of cogging torque among different structures at different PM volumes.

Structure	PM Volume (m^3)	Cogging Torque (mNm)
Non-overhang	4.26×10^{-5}	628
Conventional overhang	4.26×10^{-5}	692
Proposed structure	4.26×10^{-5}	740
Non-overhang	4.33×10^{-5}	665
Conventional overhang	4.33×10^{-5}	727
Proposed structure	4.33×10^{-5}	765

4. Conclusions

In this paper, PMs are integrated into an axial rotor to utilize the otherwise unused space on both the rotor side and the yoke side near the stator end windings. By strategically placing PMs on both sides of the stator, an effective magnetic flux path is formed, resulting in a stronger magnetic field. This enhanced field interacts with the stator's electromagnetic field to produce greater torque. The proposed structure is compared with a conventional design using the same volume of PM material, demonstrating the advantages of the new configuration. Additionally, a magnetic equivalent circuit (MEC) model of the machine is developed and validated through Finite Element (FE) analysis. The results confirm that incorporating the axial–radial rotor in a PM machine increases the average airgap magnetic field, thereby enhancing torque performance. Moreover, optimization of the proposed design is performed to enhance torque/PM , and the analysis of the proposed structure in terms of efficiency, power factor, losses, torque ripple, core loss, flux linkage, and back-EMF is also presented in this study.

Author Contributions: Conceptualization, S.Y.; methodology, S.Y.; software, S.Y.; validation, S.Y.; formal analysis, S.Y.; investigation, S.Y.; writing—original draft preparation, M.M.; writing—review and editing, M.M. and P.R.; supervision, P.R.; project administration, P.R. All authors have read and agreed to the published version of the manuscript.

Funding: This research received no external funding.

Data Availability Statement: The data presented in this study are available on request from the corresponding authors. The data are not publicly available due to ongoing related research.

Conflicts of Interest: The authors declare no conflicts of interest.

List of Symbols

B_r	Magnet remanence
θ	Rotor angular position
w_{mor}	Outer arc width of each PM on the radial rotor
w_{mir}	Inner arc width of each PM on the radial rotor
w_{fir}	Inner arc width between adjacent PM poles on the radial rotor
w_{for}	Outer arc width between adjacent PM poles on the radial rotor
w_{mai}	Arc width of each PM on the rotor side axial rotor
w_{fai}	Arc width between adjacent PM poles on the rotor side axial rotor
w_{may}	Arc width of each PM on the yoke side axial rotor
w_{fay}	Arc width between adjacent PM poles on the yoke side axial rotor
α_p	Magnet coverage ratio
p	Number of pole pairs
R_r	Radial rotor radius
R_m	Radial magnet radius
R_s	Radial stator radius
R_{rai}	Axial rotor radius at the rotor side
R_{rao}	Axial rotor radius at the yoke side
R_{mai}	Axial magnet radius at the rotor side
R_{mao}	Axial magnet radius at the yoke side
g_r	Radial airgap length
g_a	Axial airgap length in rotor side
g_c	Axial airgap length in yoke side
l_{st}	Stack length
l_{mo}	Radial rotor PM length
l_{mai}	Axial rotor PM length in the rotor side
l_{mao}	Axial rotor PM length in the yoke side
h_1	Axial rotor PM height

μ_r	Relative magnetic permeability
dz	Derivative with respect to the z-dimension

References

1. Wang, K.; Zhu, Z.; Ombach, G.; Chlebosz, W. Average torque improvement of interior permanent-magnet machine using third harmonic in rotor shape. *IEEE Trans. Ind. Electron.* **2013**, *61*, 5047–5057. [CrossRef]
2. Hu, P.; Wang, D.; Jin, S.; Wei, Y.; Chen, C.; Lin, N.; Zhang, Q.; Wu, X.; Zhu, H.; Sun, F. The modified model of third-harmonic shaping for a surface-mounted permanent-magnet synchronous motor under parallel magnetization. *IEEE Trans. Ind. Electron.* **2020**, *56*, 4847–4856. [CrossRef]
3. Suriano-Sánchez, S.I.; Ponce-Silva, M.; Olivares-Peregrino, V.H.; De León-Aldaco, S.E. A Review of Torque Ripple Reduction Design Methods for Radial Flux PM Motors. *Eng* **2022**, *3*, 646–661. [CrossRef]
4. Du, Z.S.; Lipo, T.A. High torque density and low torque ripple shaped-magnet machines using sinusoidal plus third harmonic shaped magnets. *IEEE Trans. Ind. Electron.* **2019**, *55*, 2601–2610. [CrossRef]
5. Kumar, S.; Zhao, W.; Du, Z.S.; Lipo, T.A.; Kwon, B.I. Design of ultrahigh speed axial-flux permanent magnet machine with sinusoidal back EMF for energy storage application. *IEEE Trans. Magn.* **2015**, *51*, 8113904. [CrossRef]
6. Wang, K.; Zhu, Z.; Ombach, G. Torque enhancement of surface-mounted permanent magnet machine using third-order harmonic. *IEEE Trans. Magn.* **2013**, *50*, 104–113. [CrossRef]
7. Wang, K.; Zhu, Z.; Ombach, G. Torque improvement of five-phase surface-mounted permanent magnet machine using third-order harmonic. *IEEE Trans. Energy Convers.* **2014**, *29*, 735–747. [CrossRef]
8. Zheng, Y.; Wu, L.; Zhu, J.; Fang, Y.; Qiu, L. Analysis of dual-armature flux reversal permanent magnet machines with Halbach array magnets. *IEEE Trans. Energy Convers.* **2021**, *36*, 3044–3052. [CrossRef]
9. Yousefnejad, S.; Heydari, H.; Akatsu, K.; Ro, J.S. Analysis and design of novel structured high torque density magnetic-geared permanent magnet machine. *IEEE Access* **2021**, *9*, 64574–64586. [CrossRef]
10. Yousefnejad, S.; Heidary, H.; Ro, J.S.; Amiri, E.; Afjei, S.E.; Akatsu, K. A Novel Structure of Magnetic-Geared Permanent Magnet Machine Based on Halbach Array. In Proceedings of the 2022 IEEE Kansas Power and Energy Conference (KPEC), Manhattan, KS, USA, 25–26 April 2022; pp. 1–6.
11. Jin, J.; Wang, X.; Zhao, C.; Xu, F.; Pei, W.; Liu, Y.; Sun, F. Characteristics Analysis of an Electromagnetic Actuator for Magnetic Levitation Transportation. *Actuators* **2022**, *11*, 377. [CrossRef]
12. Yousefnejad, S.; Amiri, E. Consequent-Pole Dual-Layer Axial Flux Magnetic Gear with Halbach Array. In Proceedings of the 2023 IEEE International Electric Machines & Drives Conference (IEMDC), San Francisco, CA, USA, 15–18 May 2023; pp. 1–5.
13. Zhang, Z.; Yu, S.; Zhang, F.; Jin, S.; Wang, X. Electromagnetic and structural design of a novel low-speed high-torque motor with dual-stator and PM-reluctance rotor. *IEEE Trans. Appl. Supercond.* **2020**, *30*, 5203605. [CrossRef]
14. Niu, S.; Chau, K.; Li, J.; Li, W. Eddy-current analysis of double-stator inset-type permanent magnet brushless machines. *IEEE Trans. Appl. Supercond.* **2010**, *20*, 1097–1101.
15. Chen, J.; Liu, K.; Zhou, S.; Cai, H.; Chen, Y.; Huang, C.; Zhang, D. Torque Enhancement of Surface-mounted Permanent Magnet Synchronous Machines via Axial Assisted Magnets. In Proceedings of the 2022 Second International Conference on Sustainable Mobility Applications, Renewables and Technology (SMART), Cassino, Italy, 23–25 November 2022; pp. 1–8.
16. Yeo, H.K.; Ro, J.S. Novel analytical method for overhang effects in surface-mounted permanent-magnet machines. *IEEE Access* **2019**, *7*, 148453–148461. [CrossRef]
17. Yeo, H.K.; Lim, D.K.; Jung, H.K. Magnetic equivalent circuit model considering the overhang structure of an interior permanent-magnet machine. *IEEE Trans. Magn.* **2019**, *55*, 8201404. [CrossRef]
18. Wang, X.; Fan, Y.; Chen, Q.; Wu, Z. Magnetic circuit feature investigation of a radial–axial brushless hybrid excitation machine for electric vehicles. *IEEE Trans. Transp. Electrif.* **2022**, *9*, 382–393. [CrossRef]
19. Seo, J.M.; Ro, J.; Rhyu, S.H.; Jung, I.S.; Jung, H.K. Novel hybrid radial and axial flux permanent-magnet machine using integrated windings for high-power density. *IEEE Trans. Magn.* **2015**, *51*, 8100804. [CrossRef]
20. Woo, D.K.; Lim, D.K.; Yeo, H.K.; Ro, J.S.; Jung, H.K. A 2-D finite-element analysis for a permanent magnet synchronous motor taking an overhang effect into consideration. *IEEE Trans. Magn.* **2013**, *49*, 4894–4899. [CrossRef]
21. Yeo, H.K.; Woo, D.K.; Lim, D.K.; Ro, J.S.; Jung, H.K. Analysis of a surface-mounted permanent-magnet machine with overhang structure by using a novel equivalent magnetic circuit model. *J. Electr. Eng. Technol.* **2014**, *9*, 1960–1966. [CrossRef]
22. Wu, D.; Shi, J.T.; Zhu, Z.; Liu, X. Electromagnetic performance of novel synchronous machines with permanent magnets in stator yoke. *IEEE Trans. Magn.* **2014**, *50*, 8102009. [CrossRef]
23. Qu, R.; Lipo, T.A. Analysis and modeling of air-gap and zigzag leakage fluxes in a surface-mounted permanent-magnet machine. *IEEE Trans. Ind. Electron.* **2004**, *40*, 121–127. [CrossRef]
24. Seo, J.; Seo, J.M. Analysis of an interior permanent-magnet machines with an axial overhang structure based on lumped magnetic circuit model. *J. Magn.* **2016**, *21*, 94–101. [CrossRef]

25. Seo, J.M.; Jung, I.S.; Jung, H.K.; Ro, J. Analysis of overhang effect for a surface-mounted permanent magnet machine using a lumped magnetic circuit model. *IEEE Trans. Magn.* **2013**, *50*, 8201207. [CrossRef]
26. Yeo, H.K.; Lim, D.K.; Woo, D.K.; Ro, J.; Jung, H.K. Magnetic equivalent circuit model considering overhang structure of a surface-mounted permanent-magnet motor. *IEEE Trans. Magn.* **2015**, *51*, 8201004. [CrossRef]
27. Zarko, D.; Ban, D.; Lipo, T.A. Analytical calculation of magnetic field distribution in the slotted air gap of a surface permanent-magnet motor using complex relative air-gap permeance. *IEEE Trans. Magn.* **2006**, *42*, 1828–1837. [CrossRef]

Disclaimer/Publisher's Note: The statements, opinions and data contained in all publications are solely those of the individual author(s) and contributor(s) and not of MDPI and/or the editor(s). MDPI and/or the editor(s) disclaim responsibility for any injury to people or property resulting from any ideas, methods, instructions or products referred to in the content.